

## Supporting Information

### Boosting Charge Migration Kinetics by Fe-S Bridge for Efficacious

### Photocatalytic CO<sub>2</sub> Reduction

Keda Chen,<sup>†a</sup> Lei Ran,<sup>†ab</sup> Bei Ran,<sup>c</sup> Wei Xiong,<sup>\*ae</sup> Michael K. H. Leung<sup>\*ad</sup>

a. Ability R&D Energy Research Centre, School of Energy and Environment, City University of Hong Kong, Kowloon Tong, Hong Kong, P. R. China.

b. State Key Laboratory of Fine Chemicals, Frontiers Science Center for Smart Materials Oriented Chemical Engineering, School of Chemical Engineering, Dalian University of Technology, Dalian 116024, P. R. China.

c. Institute of Regulatory Science for Medical Devices, Sichuan University, Chengdu 610064, P.R. China.

d. State Key Laboratory of Marine Pollution, City University of Hong Kong, Hong Kong, P. R. China

e. Key Laboratory of Industrial Ecology and Environmental Engineering (Ministry of Education), School of Environmental Sciences and Technology, Dalian University of Technology, Dalian 116024, P. R. China

<sup>†</sup> Keda Chen and Lei Ran contributed equally to this work.

\*To whom correspondence should be addressed. E-mail: xiongwei@dlut.edu.cn (W. Xiong),  
mkh.leung@cityu.edu.hk (M. Leung).

#### Note S1.

#### Chemicals.

Iron chloride hexahydrate (FeCl<sub>3</sub>·6H<sub>2</sub>O, >99.0%purity), sodium acetate (CH<sub>3</sub>COONa, >99.0%purity), Melamine (C<sub>3</sub>H<sub>6</sub>N<sub>6</sub>, >99.0%purity), Triethanolamine (C<sub>6</sub>H<sub>15</sub>NO<sub>3</sub>, >78%), Ethanol (CH<sub>3</sub>CH<sub>2</sub>OH, >99.7%), Ethylene glycol (C<sub>2</sub>H<sub>6</sub>O<sub>2</sub> (EG), >99.0%) and Hydrochloric acid (HCl, 36.0-38.0%) were purchased from Sinopharm Chemical Reagent Co., Ltd. (China). Doubly distilled water was used throughout this work. All chemicals were used as received without further purification.

#### Synthesis of Fe<sub>2</sub>O<sub>3</sub>.

Pure Fe<sub>2</sub>O<sub>3</sub> nanorods were prepared by slightly modifying the previously reported method.<sup>1</sup> FeCl<sub>3</sub>·H<sub>2</sub>O (0.273 g) was dispersed in H<sub>2</sub>O (0.7 mL) and CH<sub>3</sub>CH<sub>2</sub>OH (10 mL) under magnetic stirring. Then, CH<sub>3</sub>COONa (0.8 g) was added into the solution under magnetic stirring. The mixture was then transferred to a Teflon-lined stainless-steel autoclave with

a 20 mL capacity and maintained at 180°C for 12 h. After it cooled down to room temperature, the red product was separated by centrifugation and washed with water several times.

### **Synthesis of Fe<sub>2</sub>O<sub>3</sub>/Bi<sub>19</sub>Br<sub>3</sub>S<sub>27</sub> heterojunction.**

The method for the synthesis of Fe<sub>2</sub>O<sub>3</sub>/Bi<sub>19</sub>Br<sub>3</sub>S<sub>27</sub> heterojunctions is the following. Firstly, BiBr<sub>3</sub> (5 mmol), thiourea (4.6 mmol), ethylenediaminetetraacetic acid (0.2 g) and ethanol (60 mL) were first mixed under vigorous stirring for 1h at room temperature in air. The primrose yellow suspension gradually turned into a bright yellow transparent solution. Secondly, a certain amount of Fe<sub>2</sub>O<sub>3</sub> nanoplates were added into above solution. The mixed solution was transferred into a 100 mL Teflon-lined stainless-steel autoclave. The sealed autoclave was heated at 180 °C for 72 h in an oven, and then naturally cooled to ambient temperature. Then centrifuge several times and dried under vacuum. Fe<sub>2</sub>O<sub>3</sub>/Bi<sub>19</sub>Br<sub>3</sub>S<sub>27</sub> heterojunctions marked as FO/BBS-5, FO/BBS-10, FO/BBS-20 and FO/BBS-50 were obtained. The obtained sample was ground into powder for further use. Pure Bi<sub>19</sub>Br<sub>3</sub>S<sub>27</sub> nanowires are prepared via similar process except for the absence of Fe<sub>2</sub>O<sub>3</sub> nanoplates.

### **Synthesis of defective Fe<sub>2</sub>O<sub>3</sub>/Bi<sub>19</sub>Br<sub>3</sub>S<sub>27</sub> heterojunction.**

The V-Bi<sub>19</sub>Br<sub>3</sub>S<sub>27</sub> nanowires with S and Br vacancies were synthesized using an alkali-etching strategy.<sup>2</sup> In a typical procedure, 0.2g of Fe<sub>2</sub>O<sub>3</sub>/Bi<sub>19</sub>Br<sub>3</sub>S<sub>27</sub> were added into a beaker with NaOH solution (30 ml, 0.5 mol/L) and stirred continuously for 5 min at 60°C. The obtained products were washed with deionized water and ethanol for four times and dried at 80°C for 4 h in a vacuum oven, the defective Fe<sub>2</sub>O<sub>3</sub>/Bi<sub>19</sub>Br<sub>3</sub>S<sub>27</sub> heterojunctions marked as FO/DBBS-5, FO/DBBS-10, FO/DBBS-20 and FO/DBBS-50 were obtained. Defective Bi<sub>19</sub>Br<sub>3</sub>S<sub>27</sub> nanowires are prepared via similar process except for the employment of pure Bi<sub>19</sub>Br<sub>3</sub>S<sub>27</sub> nanowires.

### **Note S2.**

### **Characterization.**

The materials were systematically analyzed by X-ray diffraction (XRD) pattern was recorded with a Bruker D8 Advance X-ray diffractometer with Cu-K $\alpha$  radiation at scan range of 10°– 90°. In-situ Fourier transform infrared (In-situ FTIR) were obtained on a Nicolet Nexus 470 spectrometer. Scanning electron microscopy (SEM) was performed through Gemini SEM 300. Transmission electron microscopy (TEM) images was obtained on FEI Tecnai G2 Spirit Twin transmission electron microscopes. The UV–vis diffuse reflection spectra (UV–vis DRS) was conducted with assistance of UV-3600 system (Shimadzu). In-situ X-ray photoelectron spectroscopy (XPS) and VB-XPS was conducted via Escalab

Xi+ (Thermo Scientific). Ex/In-situ Electron paramagnetic resonance (EPR) spectra were recorded on JEOL JESFA200 at room temperature. The steady-state photoluminescence (PL) and time-resolved transient photoluminescence (TRPL) emission spectra were tested on FLS-1000 (Edinburgh Instruments). Kelvin probe force microscopy (KPFM) characterization was performed under ambient conditions using a Bruker Dimension Fastscan. Transient absorption (TA) spectra was measured on a Helios femtosecond transient absorption spectrometer (Ultrafast Systems, LLC). The isotopic experiment was performed on a mass spectrometry (Finnigan MAT 271).

### Photocatalytic CO<sub>2</sub> reduction test.

The CO production rate was calculated using the following equation, where the  $N_{CO}$  represents the mole numbers of generated CO,  $M_{\text{photocatalyst}}$  is the quality of the photocatalyst in reaction,  $T_{\text{illumination}}$  is the illumination time.

$$C_{CO}(\text{mmol g}^{-1} \text{h}^{-1}) = \frac{N_{CO}}{M_{\text{Photocatalyst}} \times T_{\text{illumination}}}$$

The selectivity of CO production is evaluated using the following equation, Where the  $\phi_{CO}$  represents the mole numbers of generated CO,  $\phi_{H_2}$  represents the mole numbers of generated H<sub>2</sub>.

$$CO \text{ selectivity } (\%) = \frac{2\phi_{CO}}{2\phi_{CO} + 2\phi_{H_2}}$$

The turnover number (TON) was calculated by using the following equation, where V, M, and T represent as a sealed reactor volume, reactant mass, and irradiation time, respectively.  $C_{CO}$  represents concentrations of generated CO.

$$TON = \frac{\text{Number of reacted electrons}}{\text{Amount of catalyst}} = \frac{2C_{CO} \times V}{M \times T}$$

The apparent quantum efficiency (AQE) is performed under the condition as those previously described to further demonstrate the solar-to-fuel conversion efficiency over as-synthesized photocatalyst. Monochromatic lights with the wavelength of 420, 450, 550 and 650 nm are used for irradiation for 1 hour. The distance between catalyst and the light resource is at 10 cm during the photocatalytic process. The AQE value is calculated based on the following equations. where I is the measured light intensity of monochromatic light, A is the illumination area, t is the illumination time, h is the Plank constant, c is the light speed, and  $\lambda$  is the monochromatic light's wavelength, 2 represents the number of consumed electrons of CO<sub>2</sub> photoreduction for the formation of CO.

$$N = \frac{I \times A \times t \times \lambda}{h \times c}$$

$$AQE = \frac{\text{Total consumed electron numbers}}{\text{The number of incident photos}}$$

$$= \frac{2 \times \text{the number of evolved CO molecules}}{N}$$

### **<sup>13</sup>CO<sub>2</sub> isotope labelling experiment.**

To confirm that the ammonia and hydrazine detected in the photocatalytic experiments originated from dissolved CO<sub>2</sub>, further experiments were performed using <sup>13</sup>CO<sub>2</sub>. The <sup>13</sup>CO<sub>2</sub> was purchased from Wuhan Newradar Special Gas Co., Ltd. Before the photocatalytic reduction experiment, the reaction tube was charged and discharged with high-purity Ar, followed by pumping it to vacuum. Then the <sup>13</sup>CO<sub>2</sub> was purged into the system to reach atmospheric pressure. After <sup>13</sup>CO<sub>2</sub> photocatalytic reduction for 1 h under the 300 W Xe lamp, the supernatant was concentrated and the obtained <sup>13</sup>CO product was identified using through gas chromatography-mass spectrometry (GC-MS) (Bruker AVANCE NEO 600M).

### **In-situ diffuse reflectance infrared Fourier-transform spectroscopy (DRIFTS).**

The DRIFTS tests were obtained using a FTIR system with an in situ diffuse reflectance cell. In situ diffuse reflectance FTIR spectra were recorded by Nicolet iS50FT-IR spectrometer (Thermo, USA) with a designed reaction cell. The substrate lying in the center of the designed reaction cell was pre-deposited with a thin layer. Then an ultra-high vacuum pump was used to pump out all the gases in the reaction cell and adsorbed on the photocatalyst surface. A layer of water molecules which were necessary to provide protons in our functional model was pre-adsorbed on the surface through bubbling a small amount of water vapor before the large amount of molecular nitrogen was pumped in to construct a CO<sub>2</sub> atmosphere. At last, visible light was turned on and the IR signal was in situ collected through a MCT detector along with the reaction.

### **Photoelectrochemical experiments.**

All the photoelectrochemical characterizations were performed on the CHI760E electrochemical workstation in a three-electrode system with FTO glass (0.1 cm<sup>2</sup>) coated by catalyst, platinum foil and Ag/AgCl (in 3 M KCl) as the working, counter, and reference electrodes, respectively. During test, 0.5 M Na<sub>2</sub>SO<sub>4</sub> solution was used as electrolyte in all electrochemical measurements. The light source was a 300W Xe lamp with the light intensity was 100 mW cm<sup>-2</sup>. The I-t curves were measured under chopped illumination at 1.23 V versus reversible hydrogen electrode (vs. RHE). The electrochemical impedance spectroscopy (EIS) measurements were conducted over a frequency range 0.1-105 Hz.

Mott–Schottky plots of photocatalysts with the same three-electrode system were obtained under frequency of 500 and 1000 Hz. The electrode potential (vs. Ag/AgCl) was converted to ERHE by the following equations.<sup>1,2</sup>

$$E_{RHE} = E_{Ag/AgCl} + 0.059pH + E_{Ag/AgCl}^0$$

$$E_{Ag/AgCl}^0 = 0.1976V$$

where  $E_{Ag/AgCl}$  was the applied potential vs. Ag/AgCl (which is the applied bias in this work), and another is the standard electrode potential of the Ag/AgCl.

### **Femtosecond transient absorption (fs-TA) spectroscopy measurements.**

The fs-TA measurements were conducted on optical pump-probe spectroscopy with a modelocked Ti-sapphire laser amplifier (Spectra-Physics) as the source of femtosecond radiation (800 nm, 35–40 fs, 1 kHz, average power of 4 W). Home-built pump-probe setup was performed to capture the corresponding transient absorption spectra and kinetics with using Optical Parametric Amplifier (TOPAS, Light conversion) as pump pulse. White light continuum (420–760 nm) generated in 3 mm thickness rotated CaF<sub>2</sub> plate was used as probe beam. The experimental data were fitted to a multiexponential decay function convoluted with the instrument response function.

### **Density functional theory (DFT) calculations.**

We performed the first-principles calculations in the frame of density functional theory (DFT) with the program package CASTEP,<sup>3,4</sup> using the plane-wave ultra-soft pseudopotential (PW-USPP) method and the Perdew-Burke-Ernzerhof (PBE) form of generalized-gradient approximation (GGA) exchange-correlation energy functional.<sup>5</sup> The structure optimizations of Fe<sub>2</sub>O<sub>3</sub> and defective Bi<sub>19</sub>Br<sub>3</sub>S<sub>27</sub> with Br-S vacancy have been carried out using means of the Broyden-Fletcher-Goldfarb-Shanno (BFGS) algorithm by allowing all atomic positions to vary and relaxing lattice parameters. They would stop until the total energies were converged to 10<sup>-5</sup> eV/atom, the forces on each unconstrained atom were smaller than 0.03 eV/Å, the stresses were lower than 0.05 GPa and the displacements were less than 0.001 Å. The plane-wave cutoff, E<sub>cut</sub>, was chosen to 340 eV. The k-point meshes of 6×6×6 and 1×1×2 were used for Brillouin zone (BZ) sampling for Fe<sub>2</sub>O<sub>3</sub> and defective Bi<sub>19</sub>Br<sub>3</sub>S<sub>27</sub> with Br-S vacancy, respectively.

Supplementary Figures and Tables.

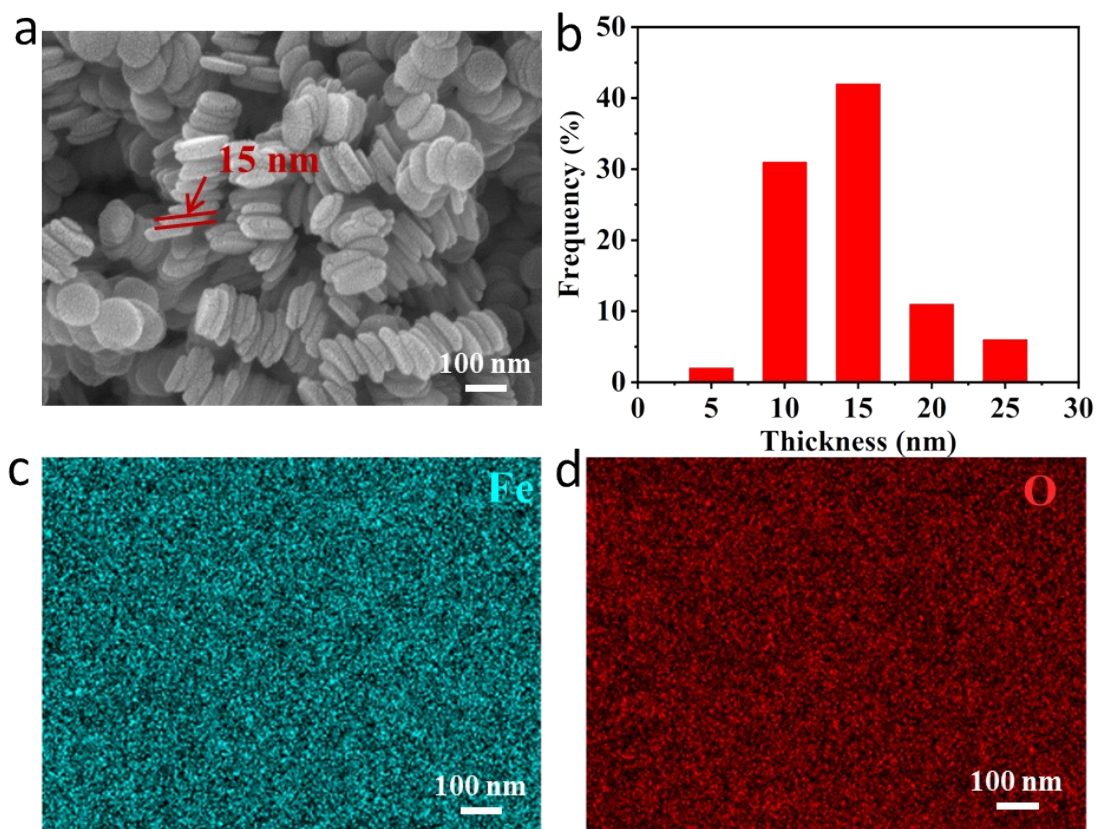


Fig. S1. SEM image, histogram of thickness and EDX elemental mapping images of Fe and O in FO.

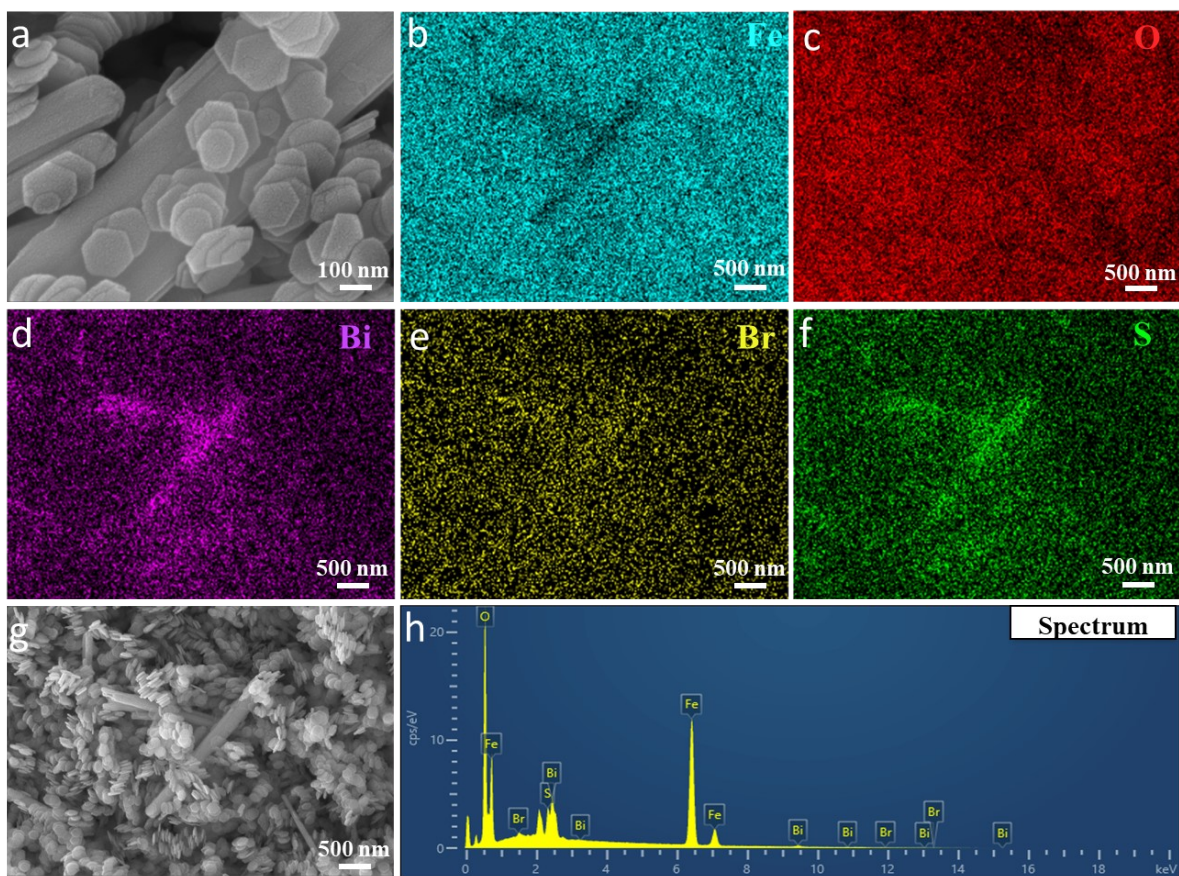


Fig. S2. SEM images, EDX elemental mapping images and EDS spectrum of Fe, O, Bi, Br, and S in FO/DBBS.

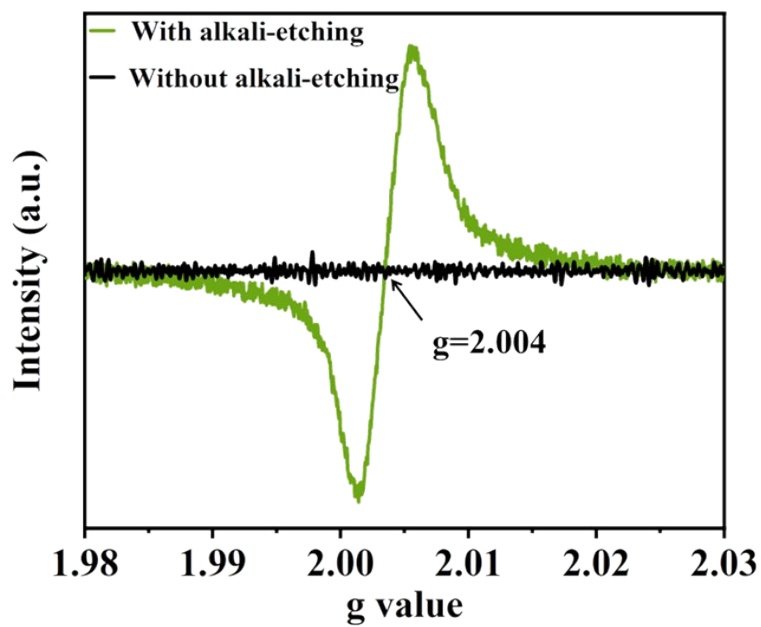


Fig. S3. EPR spectra of FO/DBBS prepared with alkali-etching and sample without alkali-etching.

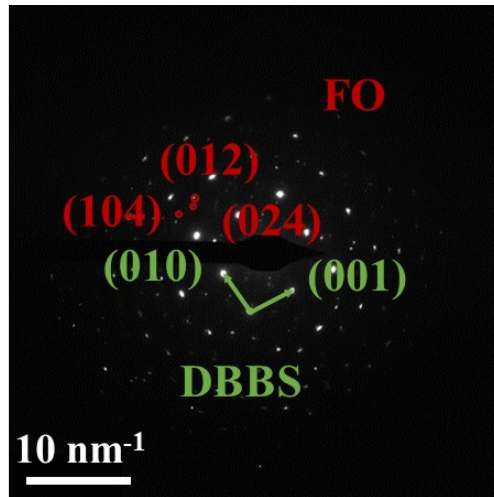


Fig. S4. SAED image of FO/DBBS.

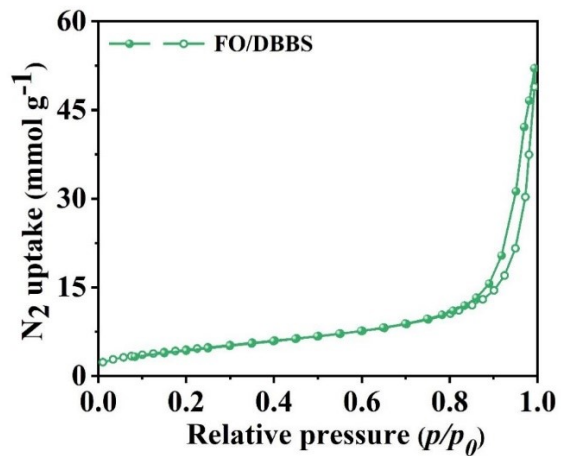


Fig. S5. N<sub>2</sub> adsorption-desorption isotherms of FO/DBBS.

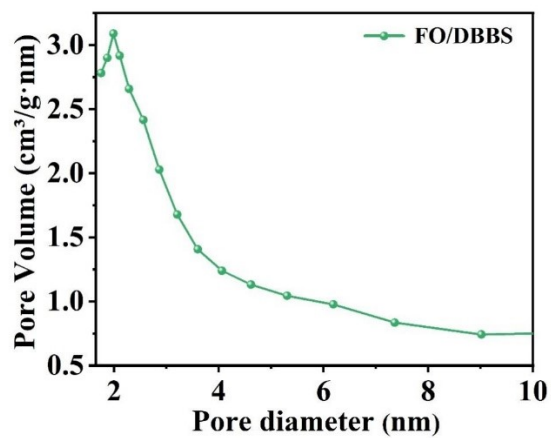


Fig. S6. Pore size distribution curves of FO/DBBS.

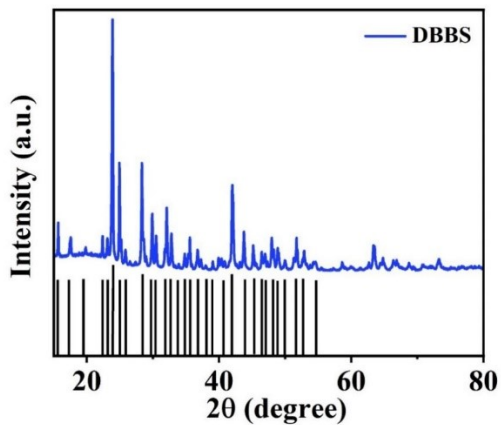
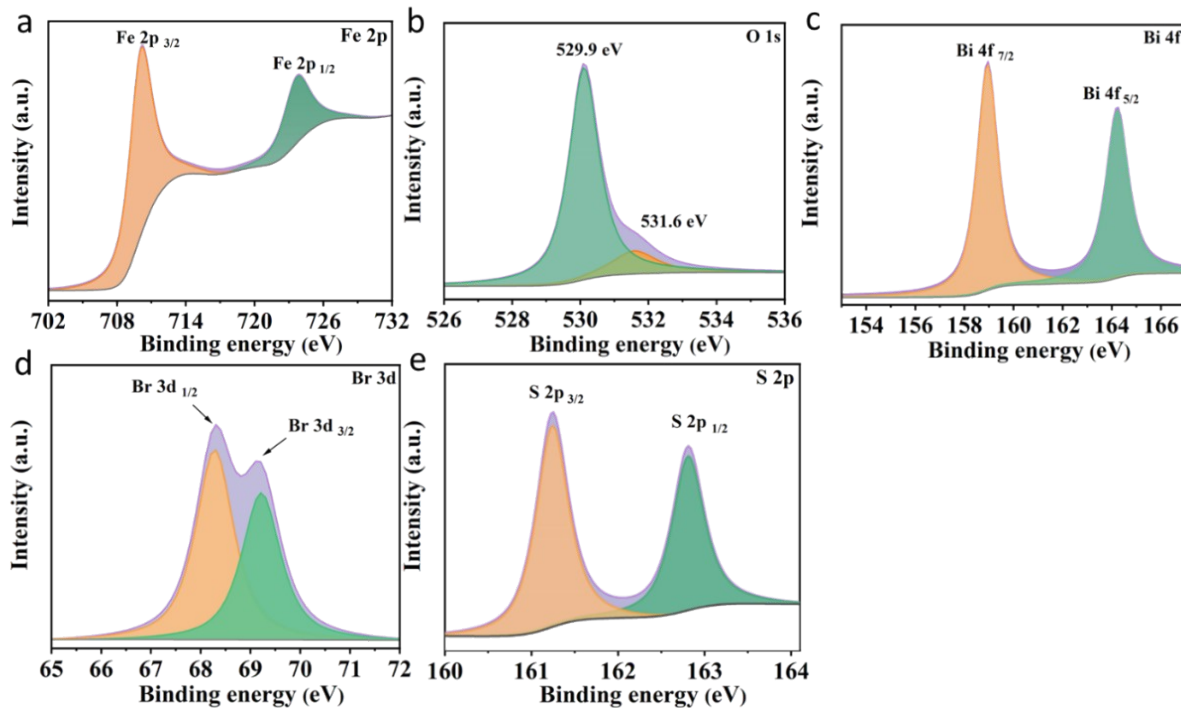
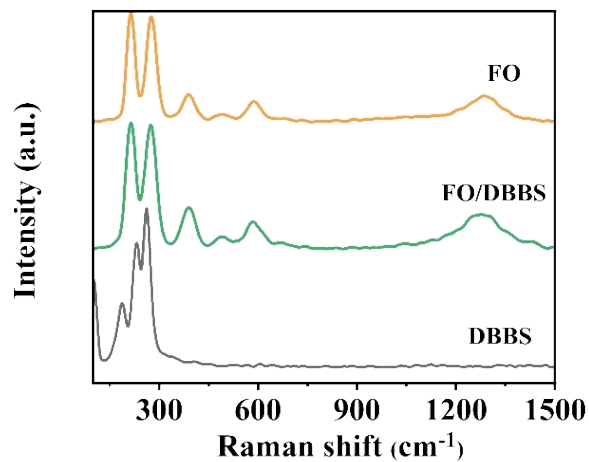


Fig. S7. XRD patterns of DBBS.



**Fig. S8.** X-ray photoelectron spectroscopy (XPS) spectra of (a) Fe 2p, (b) O 1s, (c) Bi 4f, (d) Br 3d, (e) S 2p for FO/DBBS.

The XPS analysis confirmed the existence of Fe with binding energy of around 711.7 and 723.5 eV (Fig. S8a), ascribed to Fe<sup>3+</sup>. The O 1s spectra could be deconvoluted into two peaks (Fig. S8b). The characteristic peak located at around 531.6 eV could be attributed to the absorbed oxygen species, which had a higher energy than that of the Fe-O bond (529.9 eV). The Bi 4f and Br 3d regions revealed four typical peaks at 158.9, 164.2, 68.3, and 69.3 eV, corresponding to Bi 4f<sub>7/2</sub> and Bi 4f<sub>5/2</sub> states of Bi<sup>3+</sup> as well as Br 3d<sub>1/2</sub> and Br 3d<sub>3/2</sub> states of Br<sup>-</sup>, respectively (Figs. S8c and S8d). The high-resolution spectrum of S 2p (Fig. S8e) revealed that the S 2p peak of FO/DBBS can be deconvoluted into two peaks located at 161.3 and 162.8 eV, both of which are associated with Fe<sup>3+</sup>.



**Fig. S9.** Raman spectra of FO/DBBS, DBBS and FO samples.

Fig. S9 presented the Raman spectroscopy analyses, which was used to examine the structure of the as-prepared samples. The addition of DBBS altered the structure and vibrational properties of FO, indicating a strong interaction between FO and DBBS. The FO/DBBS composite exhibited the characteristic Raman shift peaks corresponding to both FO and DBBS. Notably, compared to DBBS, the FO/DBBS composite showed a pronounced signal for the Fe-S bond at approximately  $1300\text{ cm}^{-1}$ , attributed to the increased FO content in the composite.

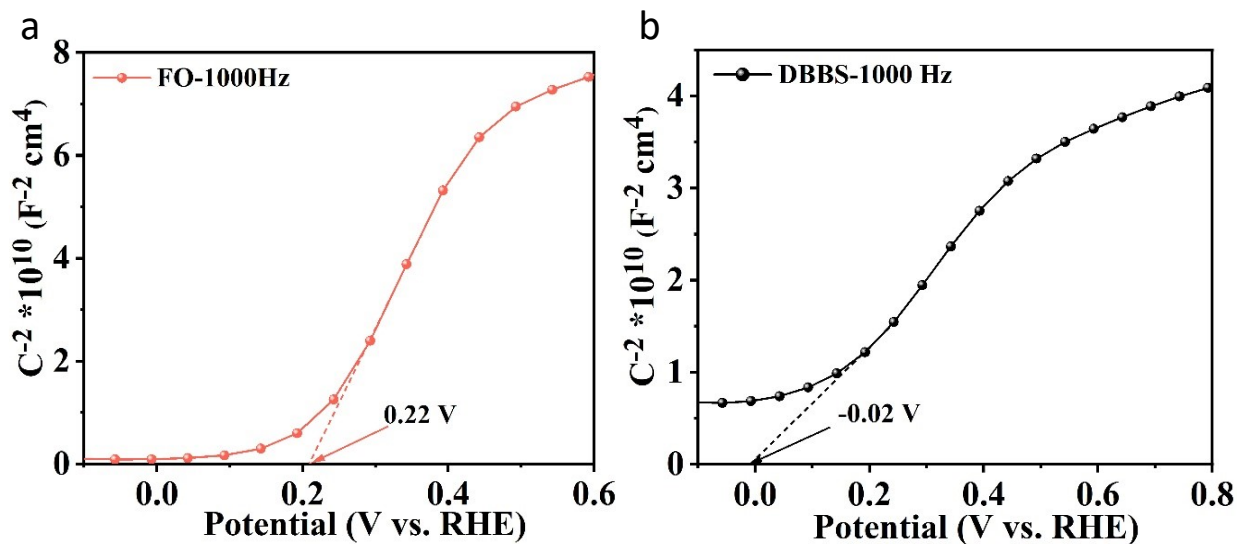


**Fig. S10.** Mott-Schottky plots of (a) FO and (b) DBBS.

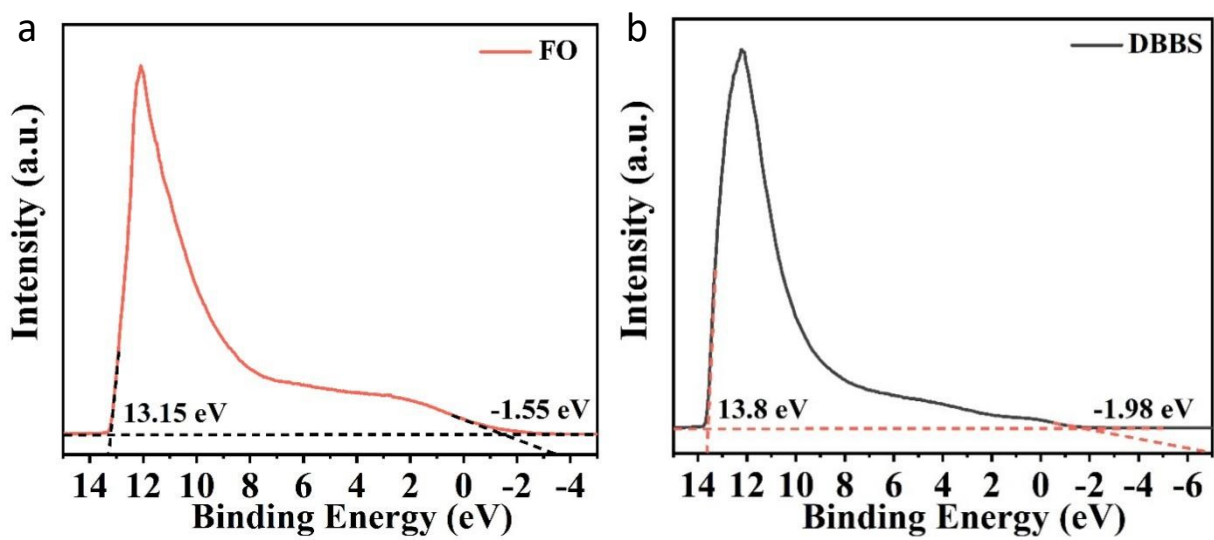


Fig. S11. UPS spectra of (a) FO and (b) DBBS.

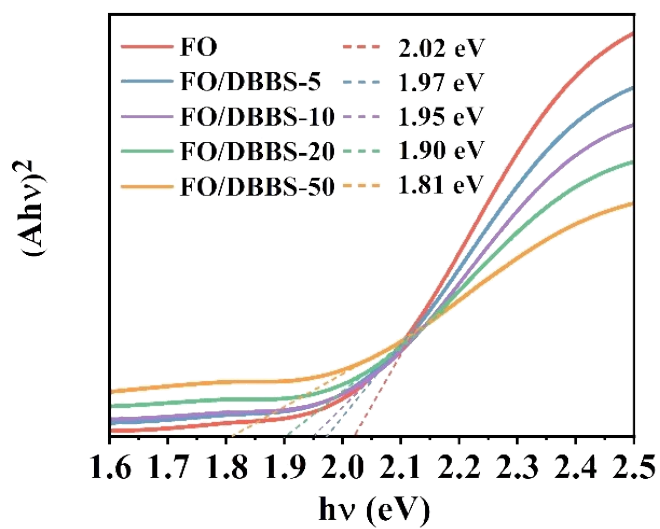
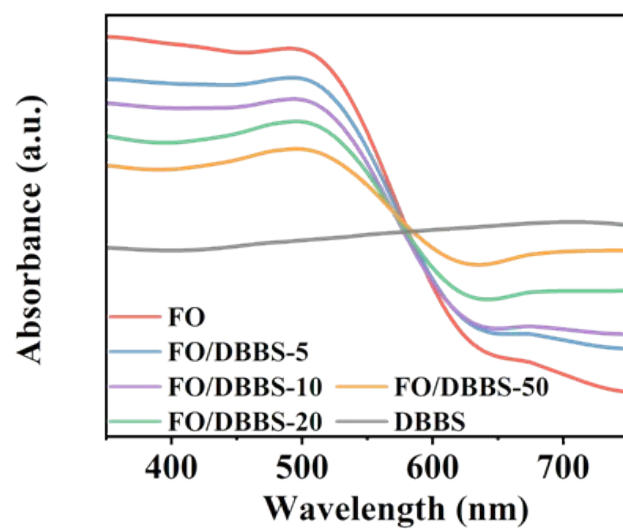


Fig. S12. Tauc plots of FO, FO/DBBS-5, FO/DBBS-10, FO/DBBS-20 and FO/DBBS-50 samples.

The band gaps ( $E_g$ ) of these samples determined from the Tauc plot (Fig. S12) were equal to 1.97, 1.95, 1.90, 1.81 and 2.02 eV for FO/DBBS-5, FO/DBBS-10, FO/DBBS-20, FO/DBBS-50 and FO, respectively.



**Fig. S13.** Ultraviolet-vis diffuse reflectance spectroscopy of FO, FO/DBBS-5, FO/DBBS-10, FO/DBBS-20 and FO/DBBS-50 samples.

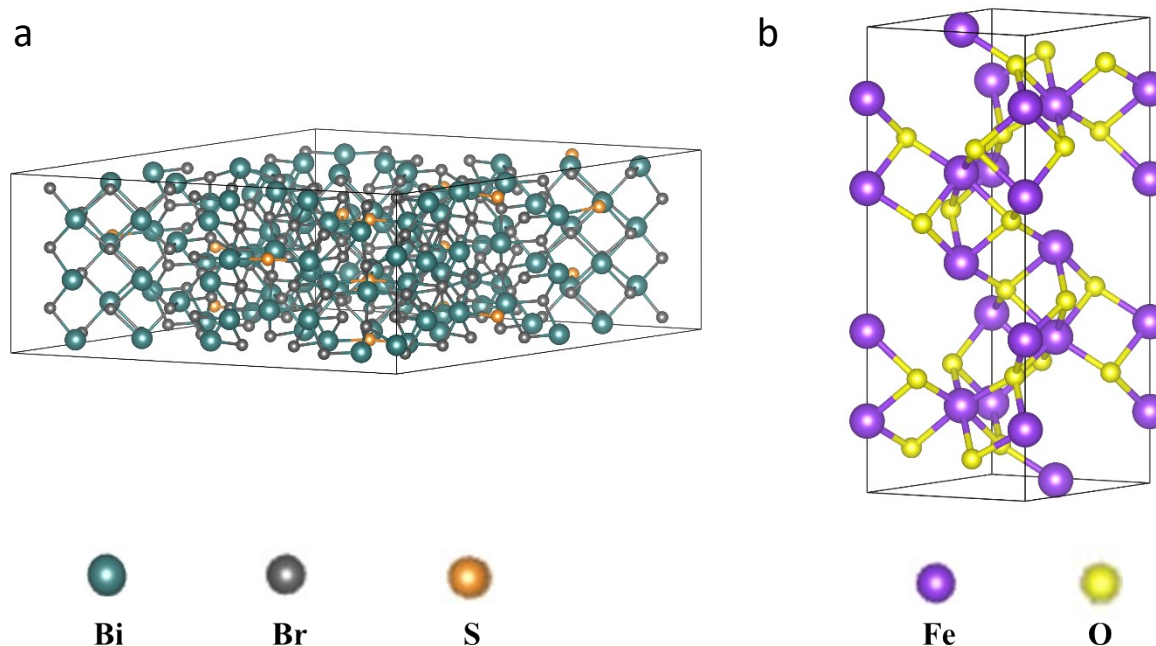


Fig. S14. Structure models of (a) DBBS and (b) FO.

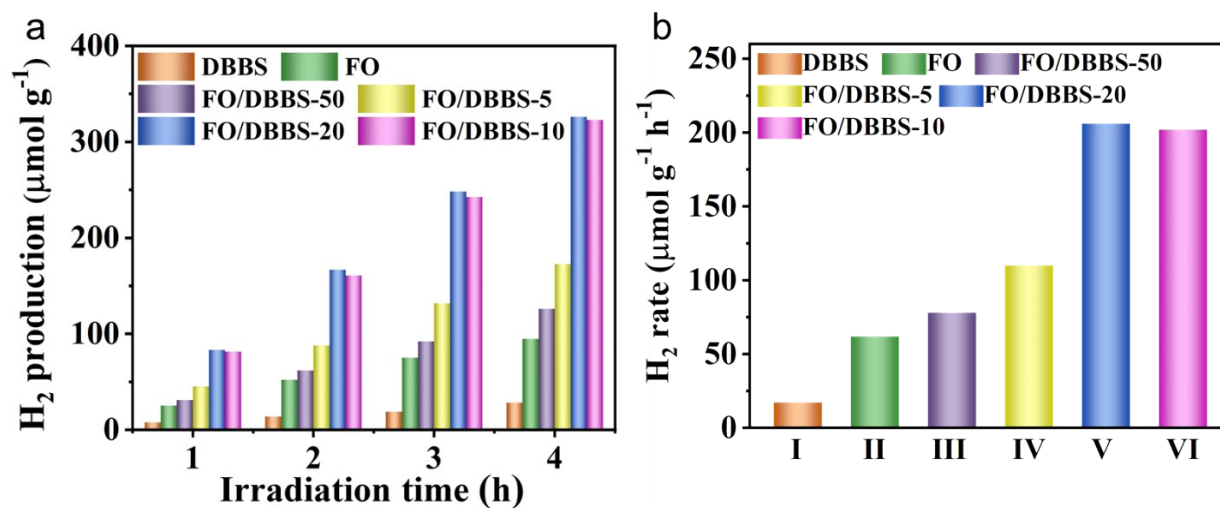


Fig. S15. (a) Photocatalytic H<sub>2</sub> evolution and (b) H<sub>2</sub> evolution rates.

Fig. S15a showed the average evolution rate of H<sub>2</sub> in the whole CO<sub>2</sub> cracking process of the catalyst under visible light ( $\lambda > 400$  nm). The H<sub>2</sub> production rate (Fig. S15b) of FO/DBBS-20 increased significantly that of DBBS and FO. Usually CO and H<sub>2</sub> could be used as syngas, but the yield of CO was much higher than H<sub>2</sub> in this paper, and syngas was principally used for producing ammonia or methanol and used as a fuel. As a comparison, CO is the basis of carbonization, which is widely used in industry and has higher application value.

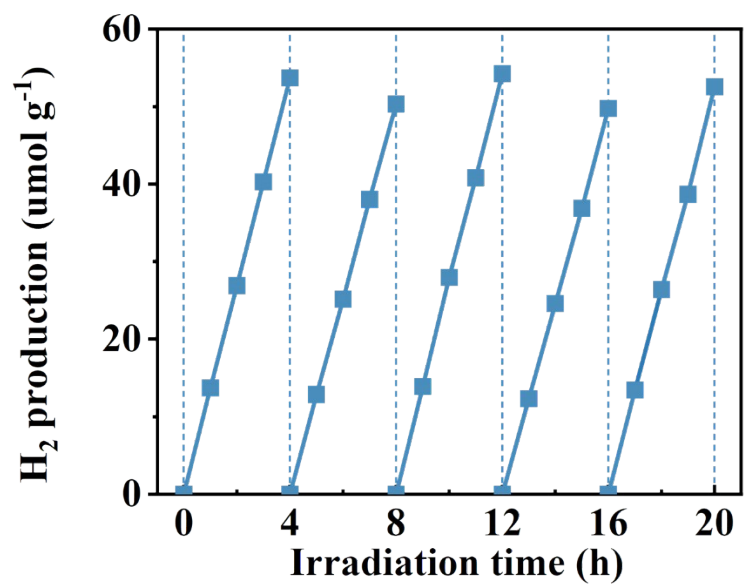


Fig. S16. H<sub>2</sub> evolution in cyclic stability tests of FO/DBBS-20 for CO<sub>2</sub> photoreduction.

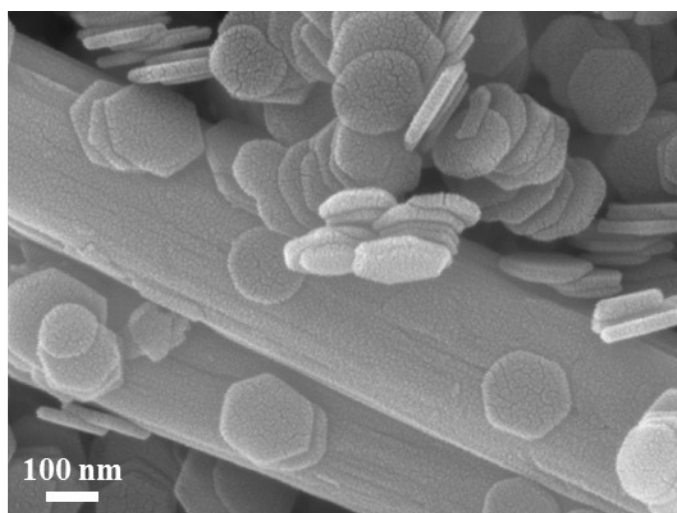


Fig. S17. FESEM image of FO/DBBS-20 after a continuous 20 h illumination.

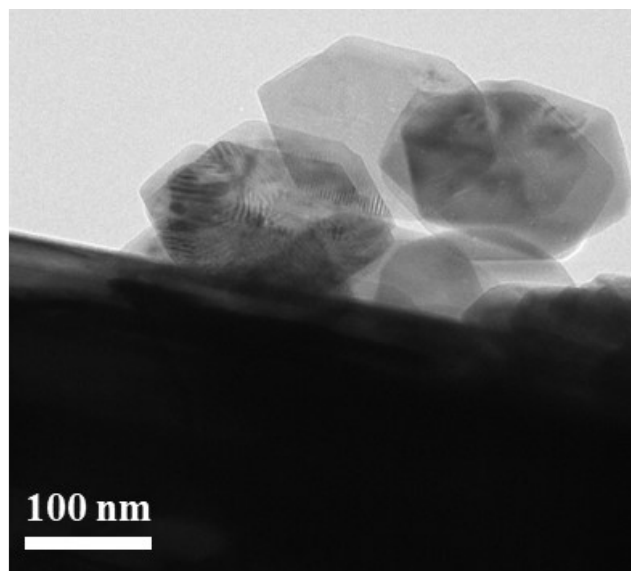


Fig. S18. TEM image of FO/DBBS-20 after 20 h cyclic stability test.

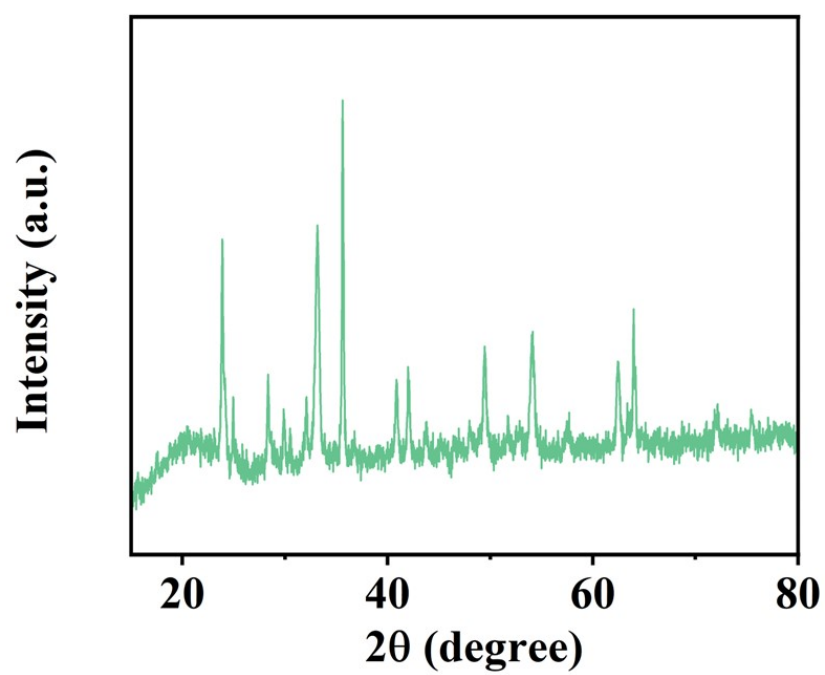
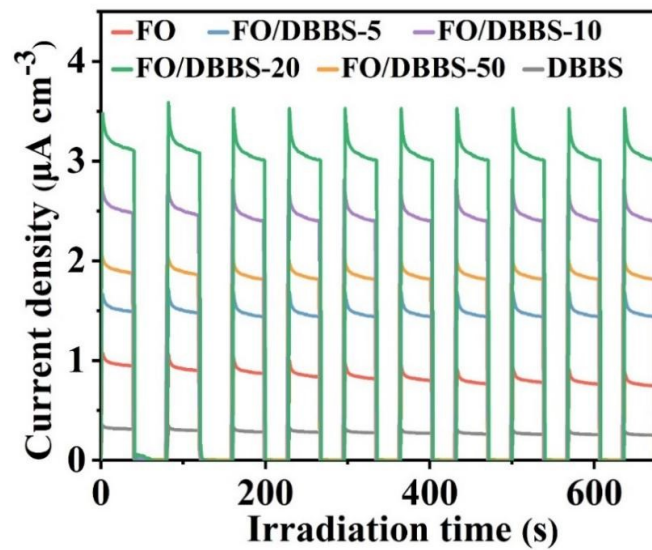
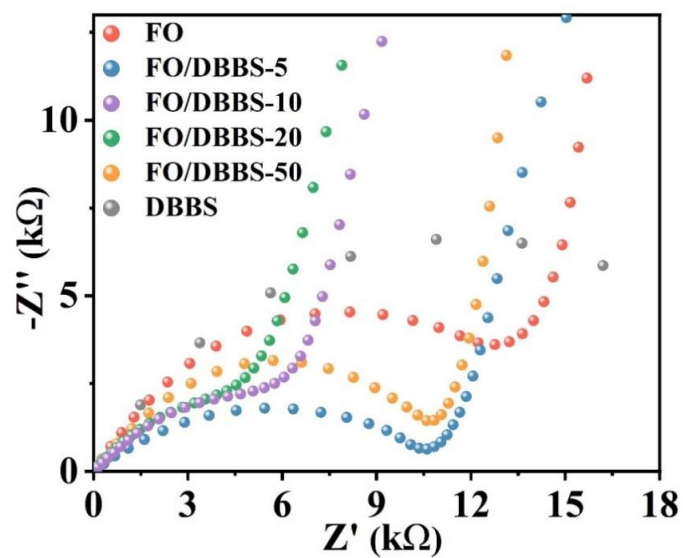


Fig. S19. XRD image of FO/DBBS-20 after 20 h cyclic stability test.



**Fig. S20.** Transient photocurrent densities under visible light irradiation in 0.5 M  $\text{Na}_2\text{SO}_4$  electrolyte solution at an applied potential of 0.5 V vs. Ag/AgCl electrode.



**Fig. S21.** Electrochemical impedance spectroscopy (EIS) Nyquist plots of samples under light illumination.

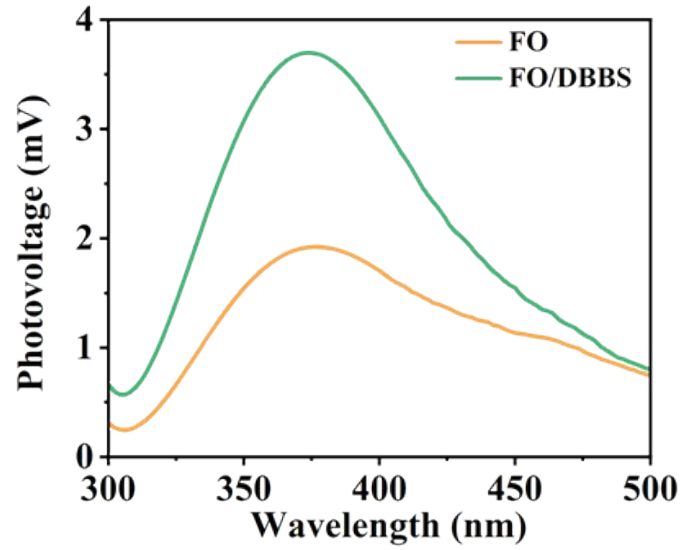


Fig. S22. SPV spectra of FO/DBBS and FO.

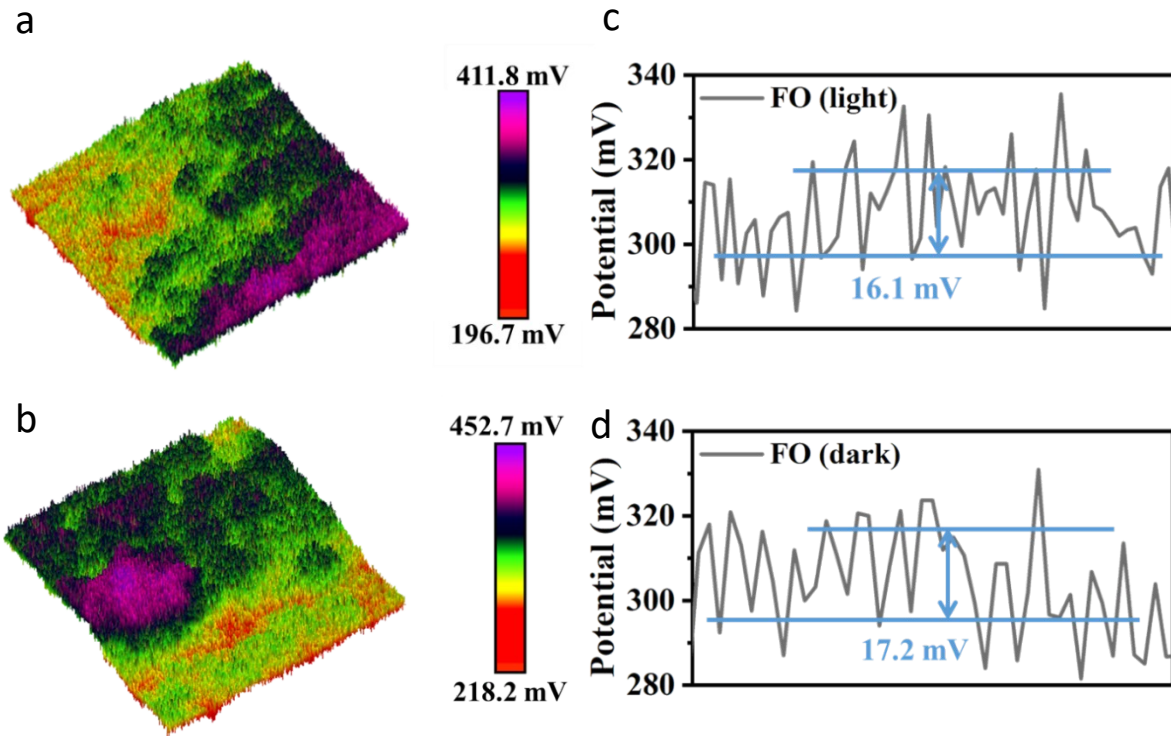


Fig. S23. 3D surface potential distribution of (a) FO under light, and (c) corresponding line-scanning surface potential profile. (b) FO in darkness, and (d) corresponding line-scanning surface potential profile.

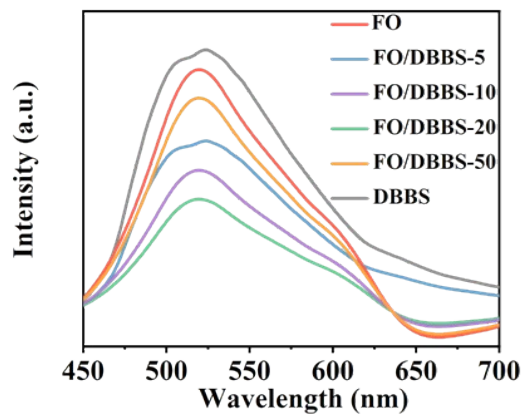


Fig. S24. Steady-state photoluminescence spectra of photocatalysts.

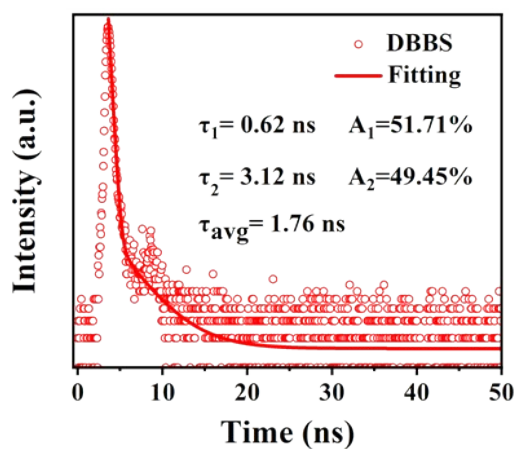


Fig. S25. Time-resolved photoluminescence (TR-PL) emission decay spectrum of DBBS.

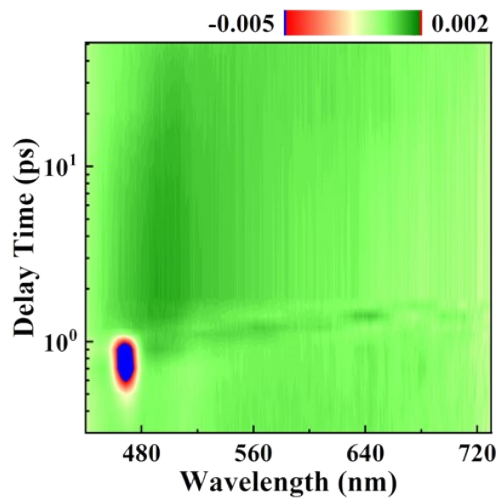


Fig. S26. Pseudocolor fs-TA spectra of DBBS.

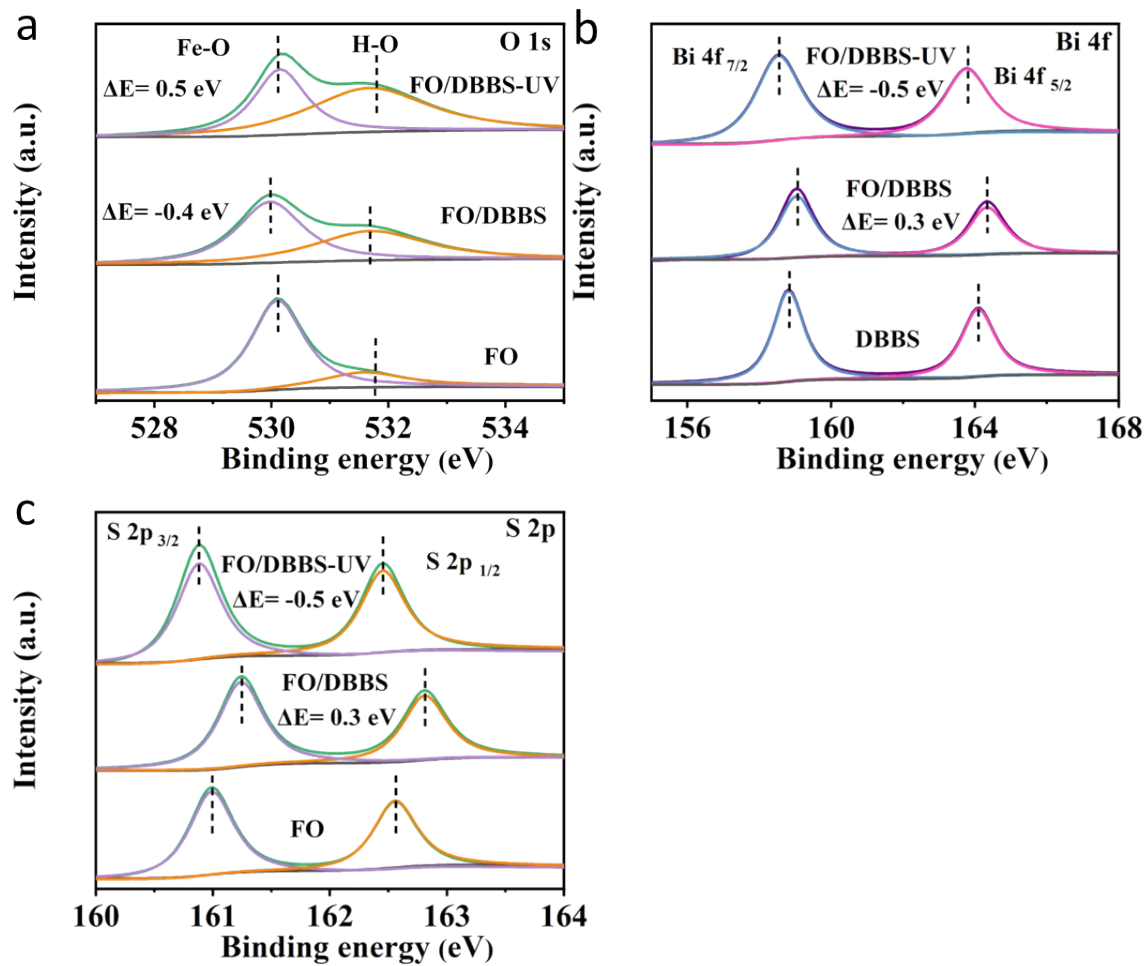


Fig. S27. High-resolution XPS spectra of (a) O 1s, (b) Bi 4f and (c) S 2p.

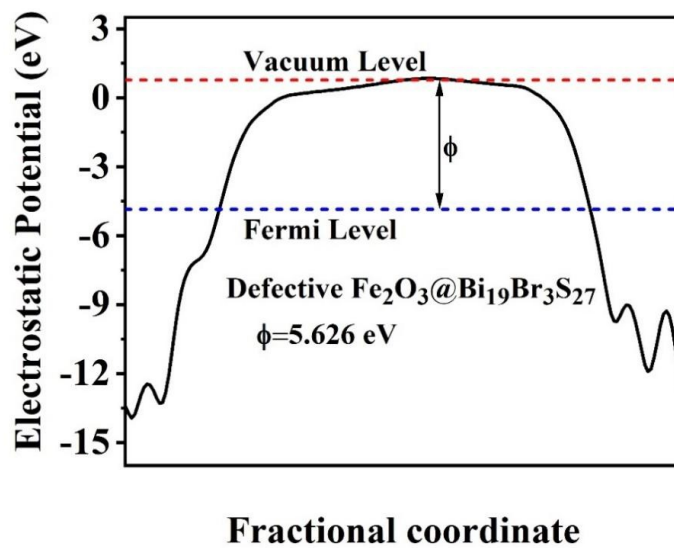


Fig. S28. Work function of FO/DBBS.

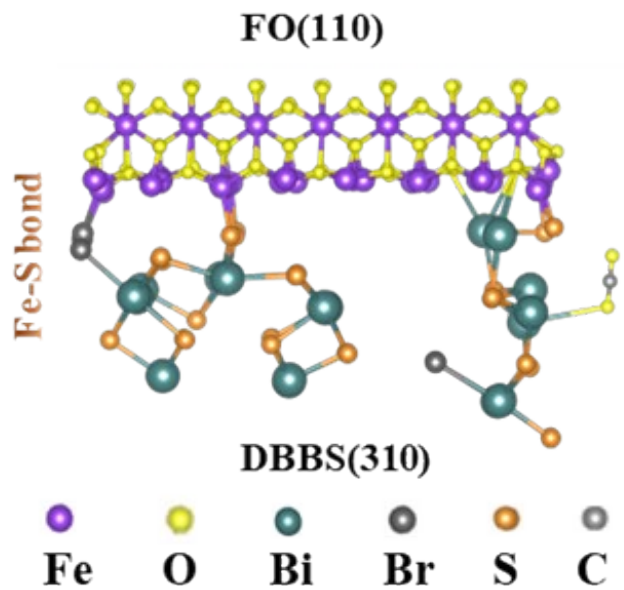


Fig. S29. Schematic model of FO/DBBS, Fe (purple), O (yellow), Bi (green), Br (dark grey), S (orange) and C (grey).

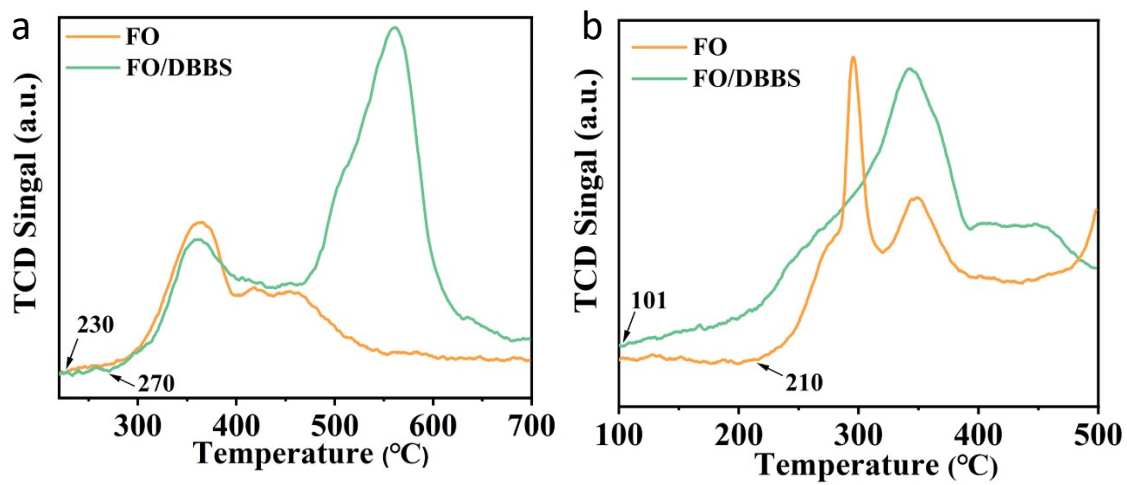
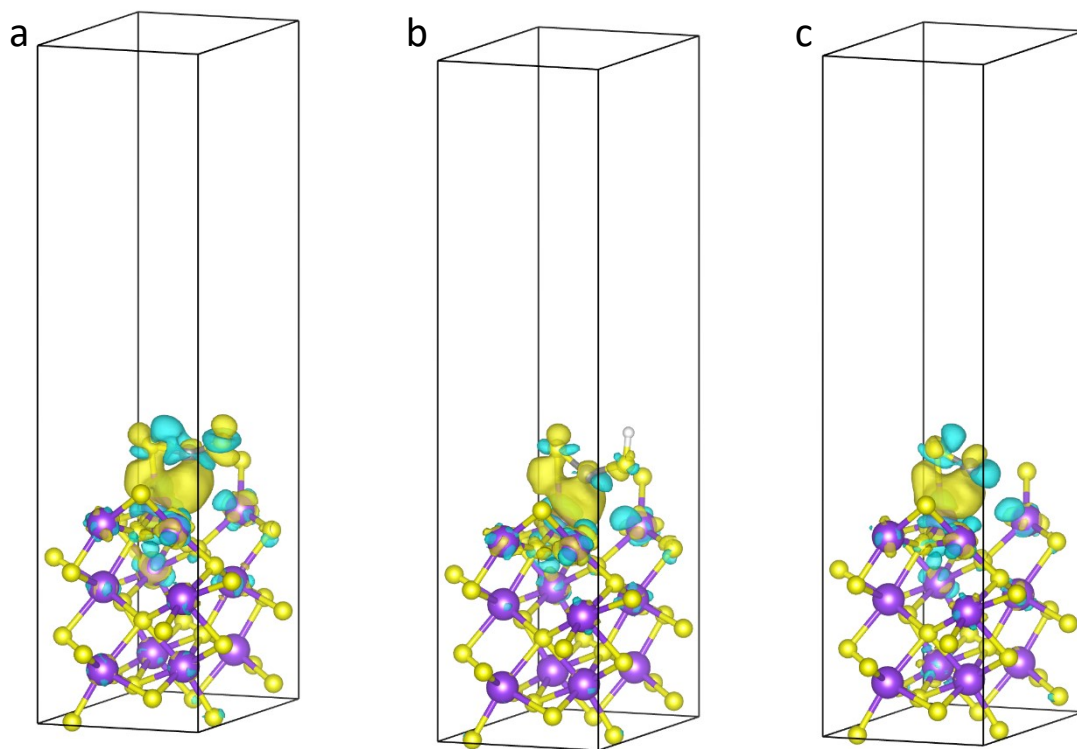
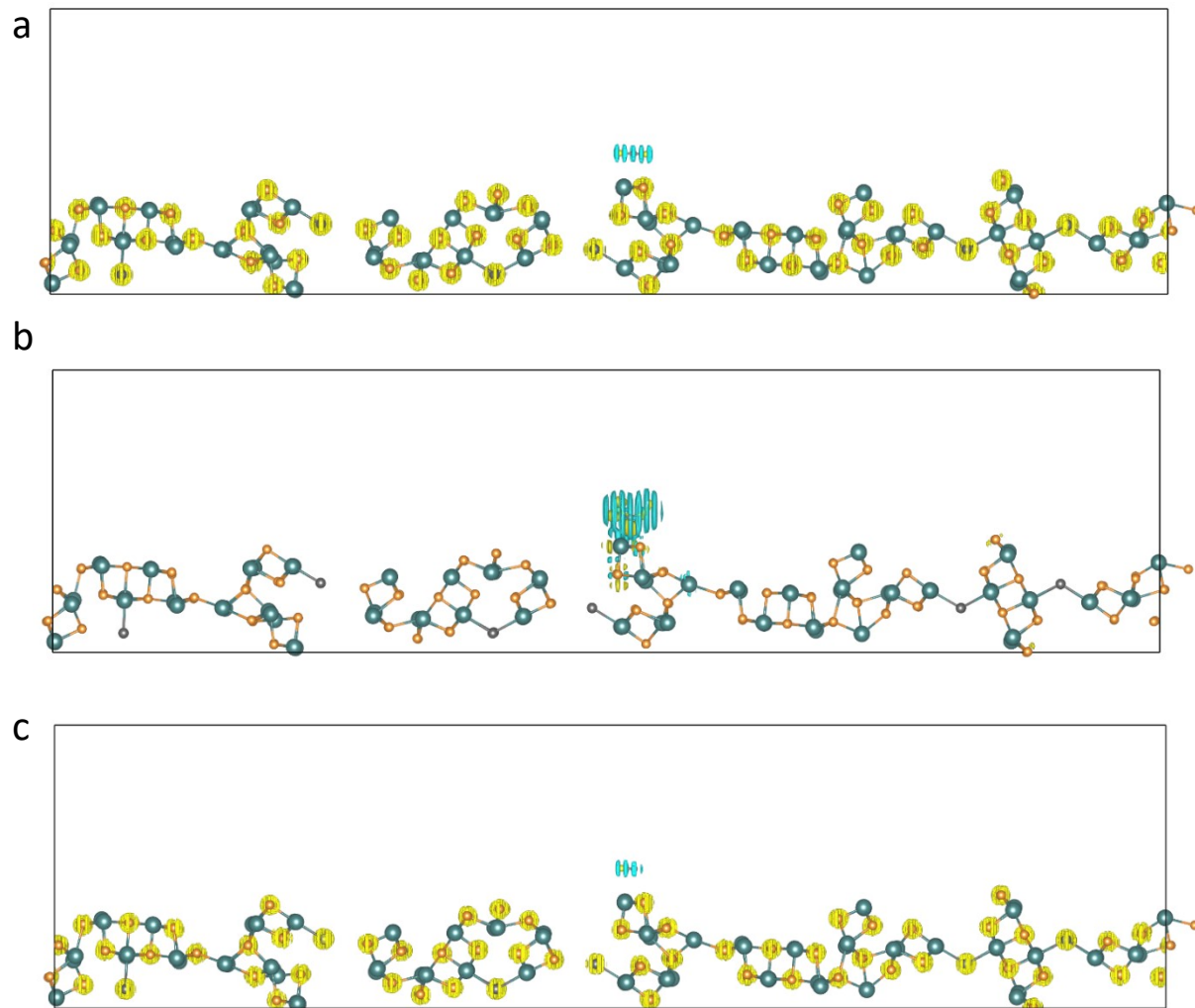


Fig. S30. (a) CO<sub>2</sub>-TPD and (b) CO-TPD spectra of FO and FO/DBBS.



**Fig. S31.** Differential charge densities of intermediates (a)  $^*CO_2$ , (b)  $^*COOH$ , and (c)  $^*CO$  over FO. Skyblue and yellow isosurfaces denote electron accumulation and depletion in FO, respectively.



**Fig. S32.** Differential charge densities of intermediates (a)  $^*CO_2$ , (b)  $^*COOH$ , and (c)  $^*CO$  over DBBS. Skyblue and yellow isosurfaces denote electron accumulation and depletion in DBBS, respectively.

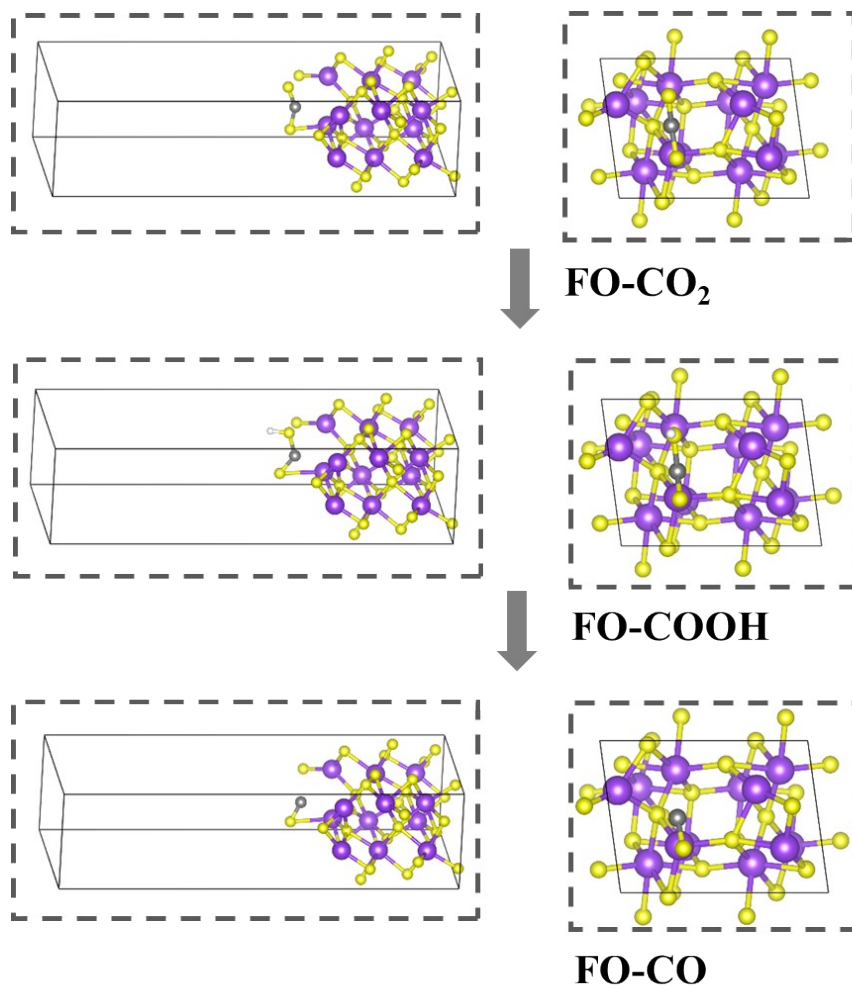


**Fig. S33.** Side and top view geometry structures of intermediates on FO.

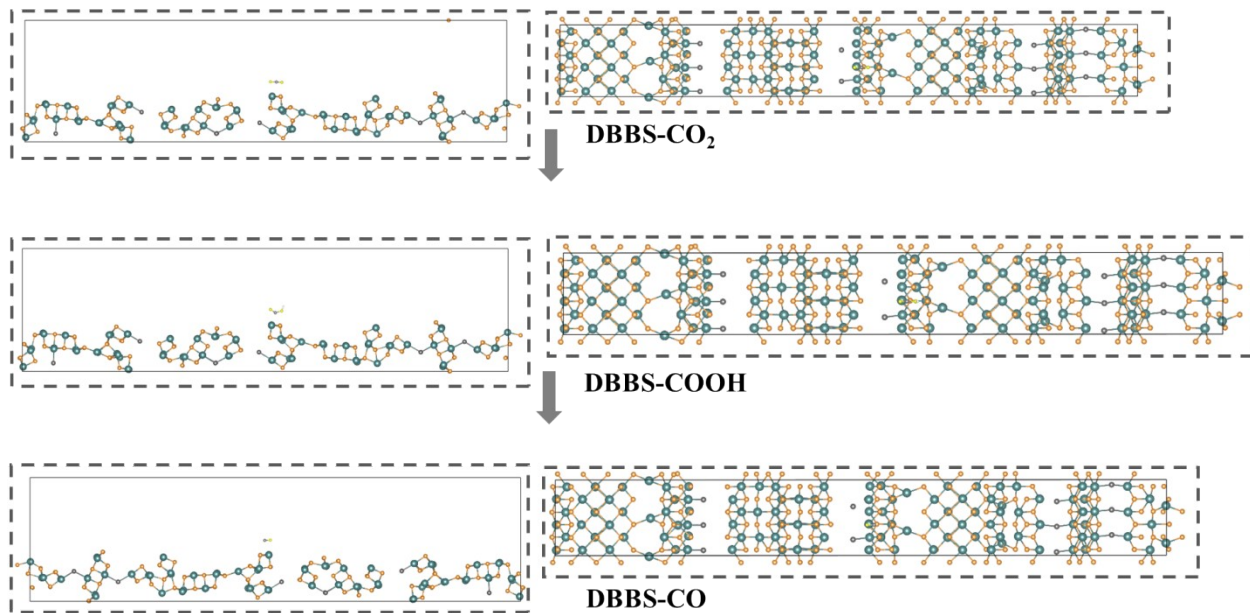


**Fig. S34.** Side and top view geometry structures of intermediates on DBBS.

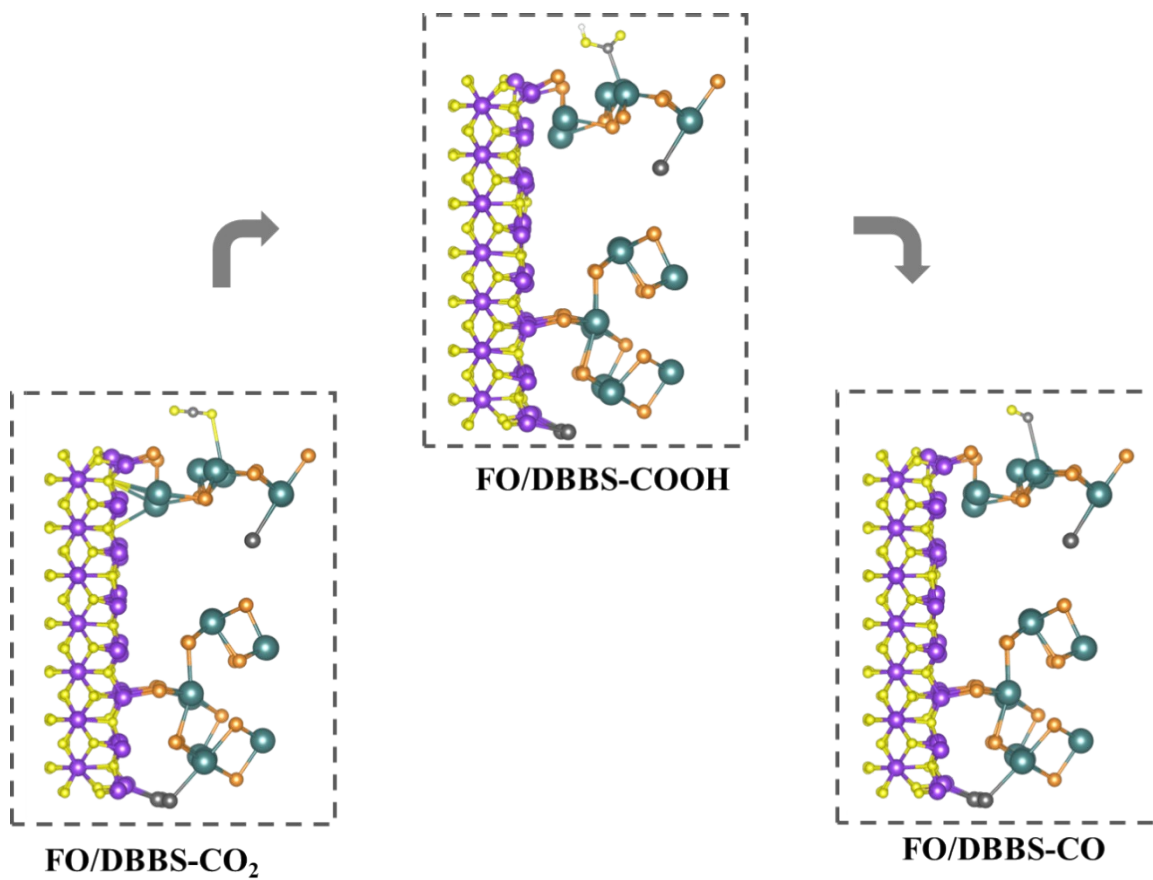


**Fig. S35.** Side view geometry structure of intermediates on FO/DBBS.

**Table S1.** Summary of typical Fe-based and Bi-based photocatalysts reported for photocatalytic CO<sub>2</sub> reduction performance.

Catalyst	Light source	Sacrificial agent	Main products	Yield of products (μmol g <sup>-1</sup> h <sup>-1</sup> )	Reference
V-Bi <sub>19</sub> Br <sub>3</sub> S <sub>27</sub> nanowires	300 W Xe lamp (λ ≥ 420 nm)	\	CH <sub>4</sub>	2.6	2
Cs <sub>3</sub> Bi <sub>2</sub> Br <sub>9</sub> /MCM-41	300 W Xe lamp (λ ≥ 420 nm)	TEOA	CO	17.24	6
α-Fe <sub>2</sub> O <sub>3</sub> /ZnFe <sub>2</sub> O <sub>4</sub>	300 W Xe lamp (λ ≥ 420 nm)	\	CO CH <sub>4</sub>	0.71 2.95	7
Bi <sub>19</sub> S <sub>27</sub> Br <sub>3</sub> /BiOBr	300 W Xe lamp	TEOA	CO	19.83	9
Bi <sub>3</sub> O <sub>4</sub> Cl/g-C <sub>3</sub> N <sub>4</sub>	300 W Xe lamp full-spectrum	TEOA	CO CH <sub>4</sub>	6.6 1.9	10
Bi <sub>2</sub> Se <sub>3</sub> /g-C <sub>3</sub> N <sub>4</sub>	300 W Xe lamp full-spectrum	Lactic acid	CO	8.2	11
Bi <sub>4</sub> NbO <sub>8</sub> Cl/g-C <sub>3</sub> N <sub>4</sub>	300 W Xe lamp (λ ≥ 420 nm)	\	CO	2.26	12
α-Fe <sub>2</sub> O <sub>3</sub> /GR/Bi <sub>2</sub> O <sub>2</sub> S	300 W Xe lamp (λ ≥ 420 nm)	TEOA	CO CH <sub>4</sub>	13.0 4.27	13
α-Fe <sub>2</sub> O <sub>3</sub> /LaTiO <sub>2</sub> N	300 W Xe lamp (λ ≥ 420 nm)	TEOA	CO CH <sub>4</sub>	29.0 38.0	14
Co <sub>1</sub> -C <sub>3</sub> N <sub>4</sub> @α-Fe <sub>2</sub> O <sub>3</sub>	300 W Xe lamp (λ ≥ 420 nm)	TEOA	CO	14.9	15
CsPbBr <sub>3</sub> /USGO/α-Fe <sub>2</sub> O <sub>3</sub>	300 W Xe lamp full-spectrum	TEOA	CO	147.6	16
α-Fe <sub>2</sub> O <sub>3</sub> @Por-CTF-10x/Ru(bpy) <sub>3</sub> Cl <sub>2</sub>	300 W Xe lamp (λ ≥ 420 nm)	Methylcyanide (MeCN)	CO	8.0	17
Defective Fe <sub>2</sub> O <sub>3</sub> /Bi <sub>19</sub> Br <sub>3</sub> S <sub>27</sub>	300 W Xe lamp (λ ≥ 420 nm)	TEOA	CO	365.1	This work

**Table S2.** Fitting parameters for kinetic traces for FO/DBBS and DBBS.

Catalysts	$\lambda_{\text{ex}}$ [nm]	$\lambda_{\text{probe}}$ [nm]	$\tau_1$ [ps]	$A_1$	$\tau_2$ [ps]	$A_2$	$\tau_{\text{avg}}$ [ps]
DBBS	450	770	0.205	79.2%	6.87	20.8%	2.32
FO/DBBS	450	770	0.905	61.4%	50	38.6%	7.70

**Table S3.** Calculated adsorption energies of CO<sub>2</sub> on Fe<sub>2</sub>O<sub>3</sub> (110), Bi<sub>19</sub>Br<sub>3</sub>S<sub>27</sub> (310) with Bi-Br vacancy surfaces and Fe<sub>2</sub>O<sub>3</sub> (110)@ Bi<sub>19</sub>Br<sub>3</sub>S<sub>27</sub> with Bi-Br vacancy heterojunction.

Surface	Adsorption energy (eV)
Fe <sub>2</sub> O <sub>3</sub> (110)	-0.11
Bi <sub>19</sub> Br <sub>3</sub> S <sub>27</sub> (310) with Bi-Br vacancy	-0.39
Fe <sub>2</sub> O <sub>3</sub> (110)@ Bi <sub>19</sub> Br <sub>3</sub> S <sub>27</sub> with Bi-Br vacancy heterojunction	-0.21

## Reference

- 1 Z. Zhu, H. Huang, L. Liu, F. Chen, N. Tian, Y. Zhang, H. Yu, *Angew. Chem. Int. Ed.*, 2022, **61**, e202203519.
- 2 J. Li, W. Pan, Q. Liu, Z. Chen, Z. Chen, X. Feng, H. Chen, *J. Am. Chem. Soc.*, 2021, **143**, 6551.
- 3 M. Segall, P. J. Lindan, M. a. Probert, C. J. Pickard, P. J. Hasnip, S. Clark, M. Payne, *J. Phys. Condens. Matter.*, 2002, **14**, 2717.
- 4 S. J. Clark, M. D. Segall, C. J. Pickard, P. J. Hasnip, M. I. Probert, K. Refson, M. C. Payne, *Z. Kristallogr. Cryst. Mater.*, 2005, **220**, 567.
- 5 J. P. Perdew, J. A. Chevary, S. H. Vosko, K. A. Jackson, M. R. Pederson, D. J. Singh, C. Fiolhais, *Phys. Rev. B.*, 1992, **46**, 6671.
- 6 Z. Cui, P. Wang, Y. Wu, X. Liu, G. Chen, P. Gao, Q. Zhang, Z. Wang, Z. Zheng, H. Cheng, *Appl. Catal. B.*, 2022, **310**, 121375.
- 7 H. Han, T. Han, Y. Luo and Y. Jia, *Mater. Lett.*, 2023, **352**, 135181.
- 8 V. N. Gopalakrishnan, D.-T. Nguyen, J. Becerra, M. Sakar, J. M. Ahad, J. J. Jautzy, L. M. Mindorff, F. Beland, T.-O. Do, *ACS Appl. Energy Mater.*, 2021, **4**, 6005.
- 9 J. Zhao, M. Xue, M. Ji, B. Wang, Y. Wang, Y. Li, Z. Chen, H. Li, J. Xia, *Chinese J. Catal.*, 2022, **43**, 1324.
- 10 Y. Xu, X. Jin, T. Ge, H. Xie, R. Sun, F. Su, X. Li, L. Ye, *Chem. Eng. J.*, 2021, **409**, 128178.
- 11 W. W. Dong, J. Jia, Y. Wang, J. R. An, O. Y. Yang, X. J. Gao, Y. L. Liu, J. Zhao, D. S. Li, *Chem. Eng. J.*, 2022, **438**, 135622.
- 12 Y. Xu, Y. You, H. Huang, Y. Guo, Y. Zhang, *J. Hazard. Mater.*, 2020, **381**, 121159.
- 13 Y. Luo, H. Han, G. Zhang, Q. Wang and Y. Jia, *Sep. Purif. Technol.*, 2023, **314**, 123607.
- 14 J. Song, Y. Lu, Y. Lin, Q. Liu, X. Wang and W. Su, *Appl. Catal. B.*, 2021, **292**, 120185.
- 15 B. C. He, C. Zhang, P. P. Luo, Y. Li and T. B. Lu, *Green Chem.*, 2020, **22(21)**, 7552-7559.
- 16 Y.F. Mu, W. Zhang, G.X. Dong, K. Su, M. Zhang, T.B. Lu, *Small.*, 2020, **16(29)**, 2002140.
- 17 S. Zhang, S. Wang, L. Guo, H. Chen, B. Tan and S. Jin, *J. Mater. Chem. C.*, 2020, **8(1)**, 192-200.